Title

Fast Room-Temperature Mg-Ion Conduction in Clay-Like Halide Glassy Electrolytes

Permalink

https://escholarship.org/uc/item/8f47h80b

Journal

Advanced Energy Materials, 14(26)

ISSN

1614-6832

Authors

Yang, Xiaochen

Gupta, Sunny

Chen, Yu

et al.

Publication Date

2024-07-01

DOI

10.1002/aenm.202400163

Copyright Information

Fast Room-Temperature Mg-Ion Conduction in Clay-Like Halide Glassy Electrolytes

Xiaochen Yang, Sunny Gupta, Yu Chen, Dogancan Sari, Han-Ming Hau, Zijian Cai, Chaochao Dun, Miao Qi, Lu Ma, Yi Liu, Jeffrey J. Urban, and Gerbrand Ceder*

The discovery of mechanically soft solid-state materials with fast Mg-ion conduction is crucial for the development of solid-state magnesium batteries. In this paper, novel magnesium gallium halide compounds are reported that achieve high ionic conductivity of 0.47 mS cm^{-1} at room temperature. These Mg-ion conductors obtained by ball milling Mg and Ga salts exhibit clay-like mechanical properties, enabling intimate contact at the electrode–electrolyte interface during battery cycling. With a combination of experimental and computational analysis, this study identifies that the soft-clay formation is induced by partial anion exchange during milling. This partial anion exchange creates undercoordinated magnesium ions in a chlorine-rich environment, yielding fast Mg-ion conduction. This work demonstrates the potential of clay-like halide electrolytes for all-solid-state magnesium batteries, with possible further extension to other multivalent battery systems.

1. Introduction

Over the last few decades, lithium-ion battery technology has advanced rapidly, resulting in diverse applications ranging from portable devices to electric vehicles and storage for power grids.[1]

X. Yang, S. Gupta, Y. Chen, D. Sari, H.-M. Hau, Z. Cai, G. Ceder
Materials Sciences Division
Lawrence Berkeley National Laboratory
Berkeley, CA 94720, USA
E-mail: gceder@berkeley.edu
X. Yang, S. Gupta, Y. Chen, D. Sari, H.-M. Hau, Z. Cai, G. Ceder
Department of Materials Science and Engineering
University of California
Berkeley, CA 94720, USA
C. Dun, M. Qi, Y. Liu, J. J. Urban
The Molecular Foundry
Lawrence Berkeley National Laboratory
Berkeley, CA 94720, USA
L. Ma
National Synchrotron Light Source II (NSLS-II)
Brookhaven National Laboratory
Upton, NY 11973, USA

However, the limited and geographically constrained lithium sources may make it challenging to satisfy the ever-growing global demand for energy-storage devices, thereby motivating the search for electrochemical energy storage with other working ions.[2,3] Magnesium (Mg) has been identified as a promising candidate because of its high theoretical anode volumetric capacity (≈3830 Ah L^{-1} vs 2046 Ah L^{-1} for Li), rich natural abundance, low reduction potential, and lower tendency for dendrite formation.[4]

One key challenge for advancing Mg battery technology is discovering Mg-ion conductive and stable electrolytes that can sustain the reversible plating and stripping of Mg without forming an ion-blocking solid electrolyte interface (SEI) on the anode surface.[5–7] Developing solid-state Mg-ion conductors, which possess better mechanical and thermal stability than conventional liquid electrolytes,[8] may be an attractive solution to this obstacle. However, achieving facile Mg-ion transport in solid-state materials is generally challenging due to the high charge density of the divalent Mg cation.[9,10] While the past search for solid-state Mg-ion conductors has identified several candidates in oxides,[11,12] borohydrides,[13–15] chalcogenides,[16,17] polymers,[18,19] and metal-organic frameworks,[20] their performance still cannot fully meet the requirements for the operation of all-solid-state Mg batteries at ambient temperature.[21] For example, the early reported phosphate-based Mg-Zr-PO$_4$ system[12] exhibits an ionic conductivity of 6.1×10^{-3} S cm^{-1} at elevated temperature (800 °C), but the large activation energy (≈0.8 eV) has limited its application at ambient temperature. In borohydride materials, introducing neutral ligands (such as NH$_3$,[15] NH$_3$BH$_3$,[13] or NH$_2$CH$_2$CH$_2$NH$_2$)[14] to Mg(BH)$_4$ has been shown to be a general strategy to facilitate Mg-ion migration. The room temperature (RT) ionic conductivity of borohydride materials can reach up to 10^{-5} S cm^{-1} with such ligand substitution,[22] yet further conductivity enhancement is necessary for RT battery operation. The spinel chalcogenide MgSc$_2$Se$_4$ which was first reported in 2017[17] and recently further confirmed,[23] has some of the highest RT Mg-ion conductivity of 0.1 mS cm^{-1}, but is hampered by a high intrinsic electronic conductivity.

Good deformability is another essential prerequisite for the practical application of solid-state conductors. Unlike in a liquid cell where the electrode surface is fully immersed in the electrolyte, maintaining an intimate electrode–electrolyte contact is

challenging with a rigid solid electrolyte.[24] Specifically, the large volume change of cathode materials over the electrochemical cycling often results in poor solid-solid contact and high interfacial resistance at the cathode/electrolyte interface, severely degrading the battery performance.[25] Therefore, developing deformable solid-state conductors that can retain sufficient contact with electrodes throughout the charge-discharge cycles under minimal pressure would greatly benefit the fabrication of all-solid-state batteries.

In recent years, lithium halide materials (especially chlorides) have resurged as promising candidates for solid-state electrolytes, due to their favorable high RT lithium-ion conductivity, great electrochemical oxidation stability, and excellent mechanical deformability.[26–28] Beyond crystalline ternary halides, recent reports also highlight amorphous halide materials exhibiting high RT ionic conductivities.[29–31] In 2021, Jung et al. reported a new class of pliable solid electrolytes[29] xLiCl–GaF$_3$ ($2 \leq x \leq 4$) with both soft mechanical properties and high RT Li-ion conductivity of 3.6 mS cm^{-1}. Xu et al. further enhanced the RT Li-ion conductivity to 16 mS cm^{-1} by adding AlF$_3$ to form a deep eutectic system.[32] The high ionic conductivity and unique mechanical properties of these pliable solid electrolytes motivated us to investigate their potential for Mg-ion conduction.

In this work, we report on the discovery of clay-like Mg-ion solid electrolytes prepared mechanochemically from two rigid salts xMgCl$_2$–GaF$_3$. Clay formation was observed for $0.75 \leq x \leq 1.25$. The optimized 1MgCl$_2$–GaF$_3$ sample exhibits RT ionic conductivity of 0.47 mS cm^{-1}. We further confirm the viability of this system as an electrolyte by reversibly cycling an all-solid-state symmetric cell using Mg$_x$Mo$_6$S$_8$ electrodes without additional interfacial engineering. By combining spectroscopic characterization and molecular dynamics (MD) simulations with a machine learning-based interatomic potential energy model, we identify that partial anion exchange between the precursors leads to the formation of GaCl$_3$-like domains within the amorphous structure, which is responsible for the soft mechanical properties. Simulations also reveal that the partial anion exchange reaction that occurs during ball milling creates Mg-ions with heterogeneous coordination environments. The Mg-ions with a lower average coordination number and a chlorine-rich environment exhibit high mobility, which accounts for the fast Mg-ion conduction in the clay-like electrolytes. We find that, in addition to Mg^{2+}, the Cl$^-$ anions also exhibit high mobility in analogy with liquid electrolytes. This work presents a systematic investigation of the clay-like xMgCl$_2$–GaF$_3$ materials that exhibit both high RT ionic conductivity and soft mechanical properties, which can facilitate the realization of Mg-based all-solid-state batteries in an ambient environment.

2. Results

2.1. Morphology and Structure of xMgCl$_2$–GaF$_3$ Materials

To prepare a series of xMgCl$_2$–GaF$_3$ materials, MgCl$_2$ and GaF$_3$ precursors were ball-milled at varying molar ratios ($0.5 \leq x \leq 1.5$). A ball milling rate of 450 rpm and a duration of 24 h were se-

lected to facilitate the clay formation and optimize the ionic conductivity. The detailed results are presented in Figure S1 and Table S1 (Supporting Information). Products with clay-like mechanical properties formed when x is in the range of 0.75–1.25, whereas both the $x = 0.5$ and $x = 1.5$ samples remained powder-like after the mechanochemical reaction. To demonstrate the mechanical softness of the clay-like samples, we kneaded the as-synthesized 1MgCl$_2$–GaF$_3$ material into shapes of different Greek letters. As shown in **Figure 1**a, the materials could be readily rolled and bent into the designed shapes without cracking. A low glass-transition temperature (≈ -62 °C) was observed in the differential scanning calorimetry (DSC) measurement for the clay-like 1MgCl$_2$–GaF$_3$ sample (Figure S2, Supporting Information).

The scanning electron microscopy (SEM) image of the clay-like 1MgCl$_2$–GaF$_3$ sample (Figure 1b) shows a highly dense morphology with no discernible particle boundaries. In contrast, the 0.5MgCl$_2$–1GaF$_3$ and 1.5MgCl$_2$–1GaF$_3$ powder-state samples appear as inhomogeneously agglomerated particles in the SEM images, with particle size ranging from 2 to 20 μm (Figure 1c,d).

Our lab X-ray diffraction (XRD) analysis with a Cu Kα source revealed a primarily amorphous structure for all the xMgCl$_2$–GaF$_3$ ($x = 0.5$, 1 and 1.5) compositions (Figure S3, Supporting Information). The absence of sharp Bragg peaks in the lab XRD patterns indicates that only poorly (if any) crystalline phases are present in the xMgCl$_2$–GaF$_3$ samples. To further investigate whether phases with low crystallinity exist within the amorphous matrix, we performed synchrotron XRD analysis ($\lambda = 0.6199$ Å) on the three compositions. The synchrotron XRD patterns of all three samples (Figure 1e) show the peaks corresponding to MgF$_2$, which indicates that at least some anion exchange occurred during the mechanochemical synthesis. Additional peaks from GaF$_3$ can be observed in the XRD patterns of the $x = 0.5$ and 1 samples, which may be attributed to unreacted precursors. Upon increasing x, the broad peaks corresponding to MgF$_2$ gradually grow in intensity, indicating that more MgF$_2$ with better crystallinity is formed. This observation conforms to the thermodynamically favorable reaction between MgCl$_2$ and GaF$_3$ identified from the Materials Project,[33] where the anion exchange reaction 1.5MgCl$_2$ + GaF$_3$ → 1.5MgF$_2$ + GaCl$_3$ is calculated to have a negative reaction energy of -0.187 eV atom^{-1}. We note that no peaks of GaCl$_3$ can be observed in any of the XRD patterns, which may reflect its poor crystallinity after ball milling. To confirm that the crystallinity of GaCl$_3$ is sensitive to milling, MgF$_2$ and GaCl$_3$ powders were planetary-milled in a molar ratio of 1.5:1 and characterized with synchrotron XRD. The XRD pattern (Figure S4, Supporting Information) of the milled 1.5MgF$_2$–GaCl$_3$ show sharp peaks corresponding to MgF$_2$ with no peaks corresponding to GaCl$_3$, indicating that the latter's crystallinity cannot be retained during ball milling. Interestingly, we also observe that the ball-milled 1.5MgF$_2$–GaCl$_3$ sample remained in a powder state without any clay-like feature even with the extended ball milling duration of 48 h, and the resulting lab XRD shows the peaks of MgF$_2$ (Figure S5, Supporting Information). This observation indicates that a complete anion exchange system does not lead to clay formation upon ball milling, consistent with the findings for the Li-equivalent of this system.[34]
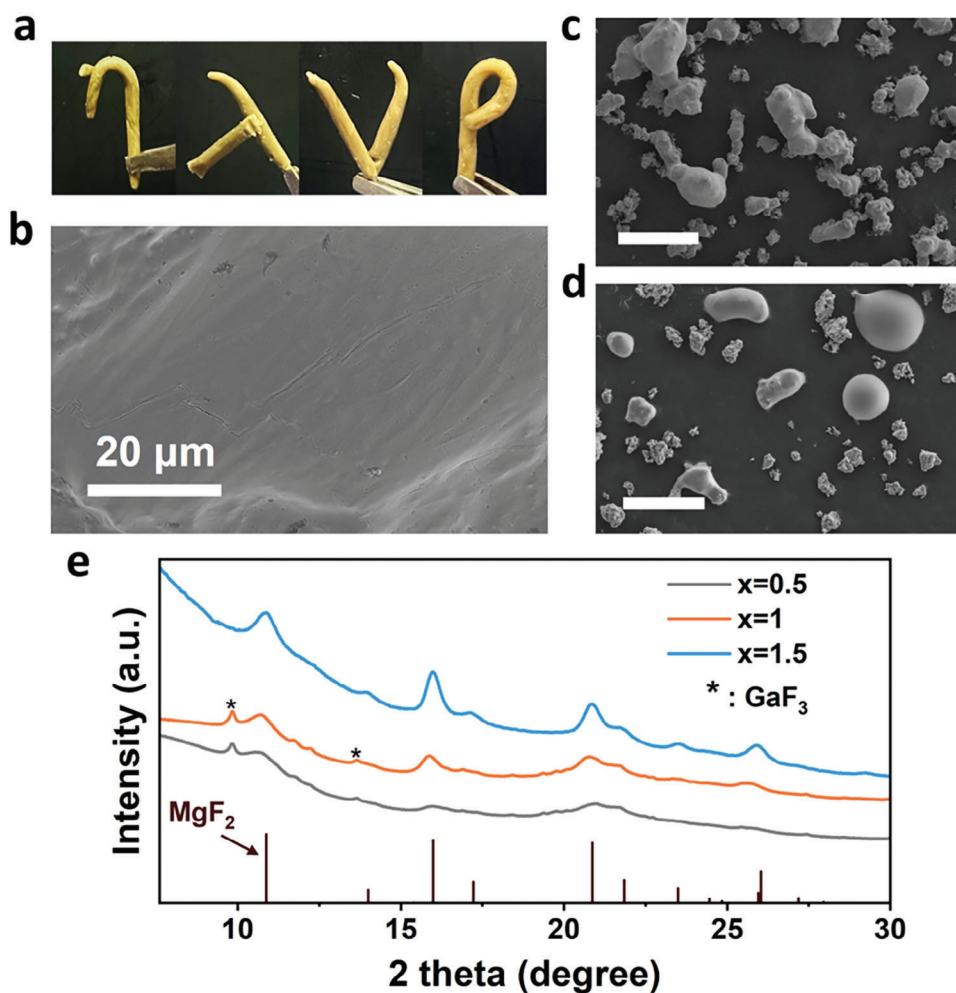
**ADVANCED
SCIENCE NEWS**

www.advancedsciencenews.com

**ADVANCED
ENERGY
MATERIALS**

www.advenergymat.de

Figure 1. a) Photographs of clay-like $1MgCl_2$–GaF_3 electrolyte kneaded into various shapes; SEM image of b) $1MgCl_2$–GaF_3 sample c) $0.5MgCl_2$–GaF_3 sample; d) $1.5MgCl_2$–GaF_3 sample (scale bar: 20 µm); e) XRD patterns of $xMgCl_2$–GaF_3 sample with x = 0.5, 1 and 1.5. The Bragg positions of MgF_2 are labeled by vertical tick marks.

2.2. Electrochemical Characterization of the Clay-Like Mg-Ion Solid Electrolytes

The Mg-ion conductivity of the $xMgCl_2$–GaF_3 samples was measured using electrochemical impedance spectroscopy (EIS). The clay-like samples were rolled into films with a thickness of 0.5–0.8 mm and punched into 5.5-mm-diameter pellets. These pellets were sandwiched between two platinum foils for EIS measurements. The samples with powder morphology were uniaxially compressed into pellets under pressure of 300 MPa with two stainless steel rods as blocking electrodes. The measured Nyquist plots at room temperature (RT, 25 °C) are shown in **Figure 2a** for clay samples and Figure 2b for powder samples. The measured RT ionic conductivities of different compositions are compared in Figure 2c. The clay samples (x = 0.75, 1, 1.25) exhibit RT ionic conductivity that is approximately three orders of magnitude higher than that of the x = 0.5 and x = 1.5 powder samples. The highest ionic conductivity of 0.47 mS cm^{-1} at RT was achieved for the composition of $1MgCl_2$–GaF_3. Figure 2d presents the Nyquist plots of the $1MgCl_2$–GaF_3 electrolyte in the

temperature range of 5 – 45 °C. The high-frequency semicircle and low-frequency linear tail in the Nyquist plot measured with the ion-blocking electrode configuration indicate that the ionic transport is much larger than electronic transport.[35] This conclusion is further confirmed by a d.c. polarization test, which indicates an RT electronic conductivity of 4.01×10^{-8} S cm^{-1} (Figure S6, Supporting Information). Fitting conductivities with an Arrhenius relation to the T-dependence of the Mg-ion conduction in $1MgCl_2$–GaF_3 gives an activation energy of 406 meV (Figure S7, Supporting Information).

When testing a symmetric Mg | $1MgCl_2$–GaF_3 | Mg cell, the impedance increased continuously (as shown in Figure S8, Supporting Information) and the cell failed after 60 h. For this reason, we constructed a symmetric cell consisting of Mo_6S_8 | $1MgCl_2$–GaF_3 | $Mg_xMo_6S_8$ (schematically shown in the inset of Figure 2e) to validate that the $1MgCl_2$–GaF_3 material can function as a solid-state electrolyte. The Chevrel phase Mo_6S_8 cathode was prepared according to a previous report,[36] and the XRD pattern of the synthesized sample matched the R$\bar{3}$ Mo_6S_8 entry in the ICSD database (Figure S9, Supporting Information). To make

ADVANCED
SCIENCE NEWS

www.advancedsciencenews.com
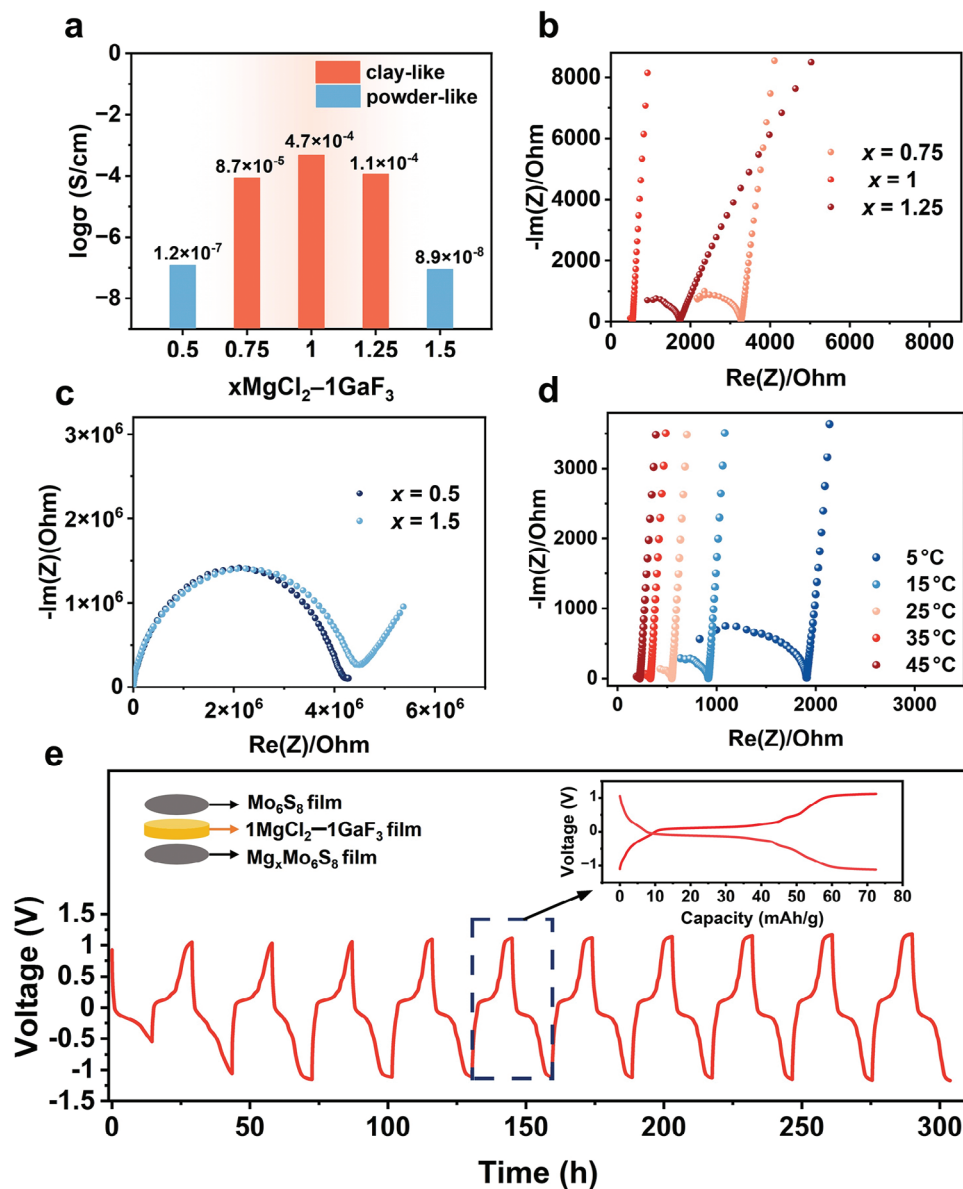
ADVANCED
ENERGY
MATERIALS

www.advenergymat.de

Figure 2. a) Nyquist plots of clay-like samples ($x = 0.75$, 1 and 1.25) from EIS measurement at RT; b) Nyquist plots of powder-like samples ($x = 0.5$ and 1.5) from EIS measurement at RT; c) RT ionic conductivities for all xMgCl$_2$–GaF$_3$ samples; d) Nyquist plots of 1MgCl$_2$–GaF$_3$ in the temperature range from 5 to 45 °C; e) Voltage profiles (voltage vs time) of Mo$_6$S$_8$ | 1MgCl$_2$–GaF$_3$ | Mg$_x$Mo$_6$S$_8$ symmetric cell. The inset Figure shows the enlarged voltage profile of the 5th cycle with the x-axis transformed from time to capacity.

the Mg$_x$Mo$_6$S$_8$ film that functions as an anode for the symmetric cell, the Chevrel phase cathode film was first discharged to −1.5 V versus an activated carbon anode in a liquid cell. The voltage profile of the liquid cell (Figure S10, Supporting Information) shows a 2nd cycle discharge capacity of ≈60 mAh g^{-1}. After the 2nd discharge cycle, the Mg$_x$Mo$_6$S$_8$ film was disassembled from the liquid cell, and the residual liquid electrolyte was removed by rinsing and drying. To confirm successful Mg intercalation, SEM energy dispersive X-ray spectroscopy (EDS) analysis was performed on the discharged Mo$_6$S$_8$ film. The ex-situ SEM–EDS result (**Table 1**) indicates a Mg atomic concentration of ≈10% in the Mg$_x$Mo$_6$S$_8$ film ($x\approx1.5$), which is consistent with the capacity measured from cycling.

Table 1. Elemental Compositions of the Mo$_6$S$_8$ film collected after the 2nd discharge cycle measured by SEM-EDS Analysis.

Atomic percentages (%)	Mg	Mo	S
Point 1	12.63	52.14	35.23
Point 2	9.44	51.71	38.85
Point 3	10.42	54.16	35.42

A symmetric Mo$_6$S$_8$ | 1MgCl$_2$–GaF$_3$ | Mg$_x$Mo$_6$S$_8$ electrode stack was sealed in a Swagelok-type cell to avoid air exposure. The Nyquist plot of the symmetric cell (Figure S11, Supporting
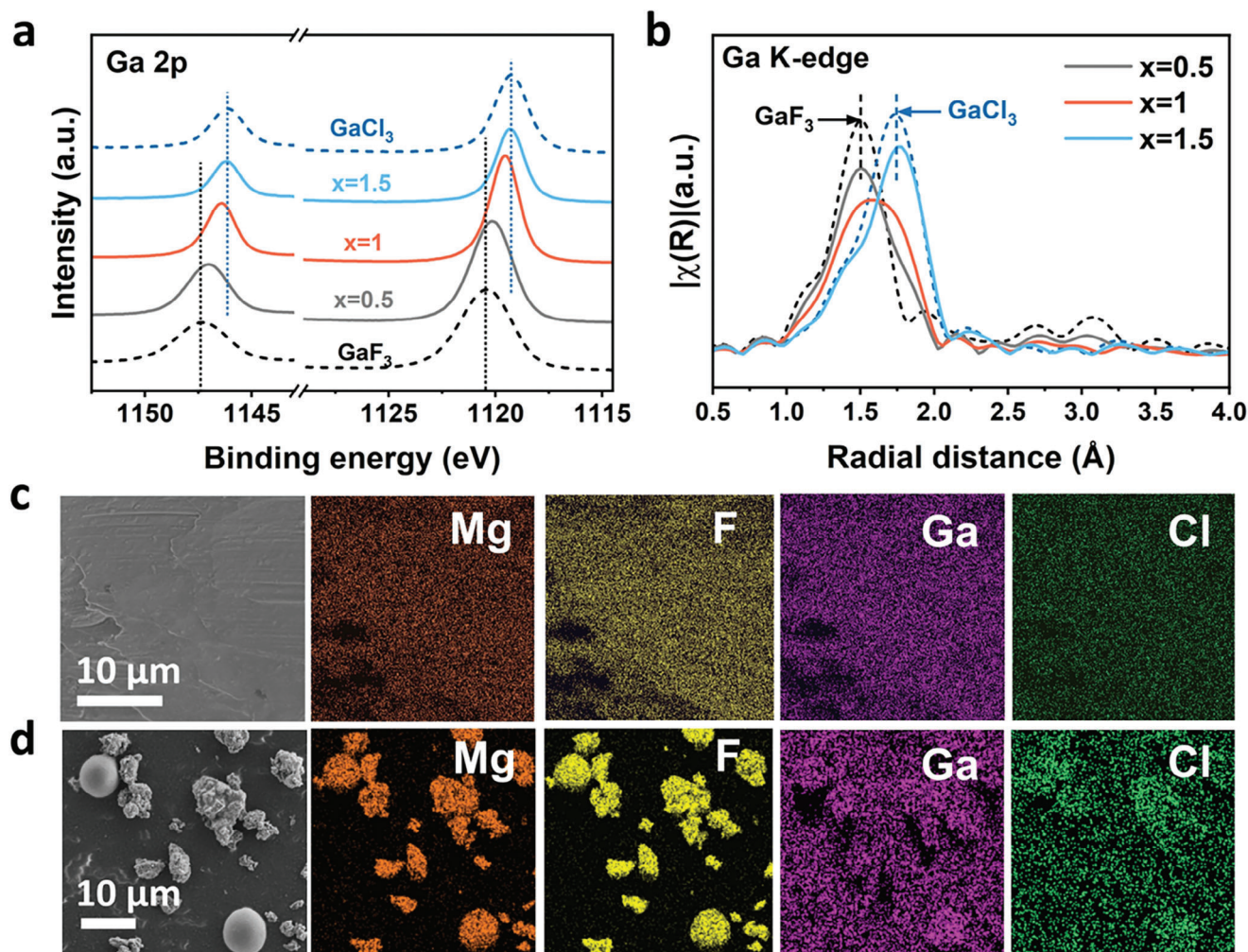
**ADVANCED
SCIENCE NEWS**

www.advancedsciencenews.com

**ADVANCED
ENERGY
MATERIALS**

www.advenergymat.de

Figure 3. a) XPS Ga 2p spectra for xMgCl$_2$–1GaF$_3$ samples (x = 0.5, 1 and 1.5) with GaF$_3$ and GaCl$_3$ (dotted line) shown as references; b) Gallium K-edge EXAFS spectra of xMgCl$_2$–1GaF$_3$ samples with GaF$_3$ and GaCl$_3$ (dotted line) shown as references; SEM EDS elemental maps of c) 1MgCl$_2$–1GaF$_3$ clay-like sample and d) 1.5MgCl$_2$–1GaF$_3$ powder-like sample.

Information) is fitted with a circuit consisting of two parallel constant phase element (CPE)/ resistors in series with a Walburg element, revealing a small electrode–electrolyte interfacial impedance of 59 Ω (the bulk impedance is 589 Ω). The voltage profile when cycling the symmetric cell at a current density of 5 mA g^{-1} and a capacity of 72.5 mAh g^{-1} is shown in Figure 2e. A voltage plateau at ≈±0.15 V is consistently observed during each charge/discharge cycle. The inset of Figure 2e, which presents the enlarged voltage profile (x-axis transformed from time to capacity) of the 5th cycle, shows a capacity of ≈55 mAh g^{-1} for the voltage plateau at ±0.15 V. In addition, a second plateau is observed at ±1.1 V, which contributes ≈15 mAh g^{-1} to the total capacity. Previous experiments have identified that the intercalation of Mg-ion into the Mo$_6$S$_8$ lattice involves a sequential occupation of inner and outer sites.[37] The plateau at ±0.15 V with a capacity of 55 mAh g^{-1} in our cell corresponds to Mg-ion intercalation into the six outer ring sites of the Mo$_6$S$_8$ structure (with a theoretical capacity of 64 mAh g^{-1}).[38] The additional plateau at ±1.1 V may be attributed to Mg-ion insertion into the six inner ring sites. The Mg-ion diffusivity for the latter process

has been reported to be low due to the ordering of Mg^{2+} and vacancies at low Mg concentration.[39] Notably, no external stack pressure was applied during the battery cycling process.

2.3. Microscopic Mechanism for Soft-Clay Formation

To explore the microscopic mechanism behind the clay formation in the xMgCl$_2$–GaF$_3$ system, we combined experimental spectroscopy and computational modeling. Three samples with varying compositions, namely x = 1(clay-like sample), x = 0.5, and x = 1.5 (powder-like samples) were characterized with X-ray photoelectron spectroscopy (XPS) and extended X-ray absorption fine structure (EXAFS). **Figure 3a** shows the Ga 2p XPS spectra of the three samples with GaCl$_3$ and GaF$_3$ as references. As the MgCl$_2$ content, x, is increased, the Ga 2p$_{1/2}$ and 2p$_{3/2}$ peaks shift toward lower binding energy. For the x = 0.5 sample, the Ga 2p peaks are close to those of pristine GaF$_3$, whereas those of the x = 1.5 sample overlap with the GaCl$_3$ peaks. Figure 3b presents the k^3 weighted Ga K-edge EXAFS spectra of xMgCl$_2$–GaF$_3$ samples

ADVANCED
SCIENCE NEWS

www.advancedsciencenews.com

ADVANCED
ENERGY
MATERIALS

www.advenergymat.de

along with those of pristine GaF_3 and $GaCl_3$ as references, which provides bulk bonding information in contrast to XPS which is surface-sensitive. The first Fourier-transformed EXAFS peak of the $x = 0.5$ sample has a similar radial distance to that of GaF_3. Upon increasing x to 1, the first peak broadens and shifts to a larger radial distance, in between that of pristine GaF_3 and $GaCl_3$. As for the $x = 1.5$ sample, the first peak in the EXAFS spectrum overlaps with that of $GaCl_3$. The EXAFS spectra (Figure 3b) indicate that in the $x = 0.5$ sample the nearest neighboring atoms of Ga are primarily fluorine, whereas in the $x = 1$ sample, the Ga atoms are bonded to both fluorine and chlorine. In the $x = 1.5$ sample, the Ga atoms have a $GaCl_3$-like local bonding environment. The XPS and EXAFS spectra suggest that the precursor GaF_3 undergoes an anion exchange reaction to replace some F with Cl anions during the mechanochemical synthesis. With a higher mixing ratio x, a higher degree of anion exchange occurs, leading to a more $GaCl_3$-like environment. The $x = 0.5$ sample exhibits only a minor amount of anion exchange with a dominant Ga-F environment remaining. The $x = 1.5$ sample exhibits a relatively complete anion exchange leading to mostly Ga-Cl environments. Both these compositions remained in a powder-like state. In contrast, only the $x = 1$ composition shows clay-like properties and has a mixed bonding environment with both F and Cl atoms coordinating the Ga cation. This suggests that partial anion exchange may be the chemical feature that contributes to the clay formation.

To further understand the connection between the extent of anion exchange and clay formation, EDS analysis was performed on the $x = 1$ and $x = 1.5$ samples. The EDS mapping of the $x = 1$ sample in Figure 3c reveals a uniform elemental distribution. Additionally, EDS point detection data on various locations reveals that the molar ratio of Mg/Ga is approximately equal to 1 (Figure S12, Supporting Information) throughout the surface, which is consistent with the mixing precursor ratio ($x = 1$). In contrast, the EDS mapping for the $x = 1.5$ sample (Figure 3d), shows a heterogeneous elemental distribution with the Mg and F concentrated into large particles. EDS analysis on these $20 – 50$ μm spherical particles gives an average molar ratio of 5 for Mg/Ga and 0.5 for Mg/F (Figure S13a, Supporting Information). This indicates that these particles have a MgF_2-dominant composition. Additionally, EDS analysis on the SEM image with higher magnification (Figure S13b, Supporting Information) shows stripe-shaped small particles consisting of only Ga and Cl. The presence of $GaCl_3$ particles from the EDS mapping agrees with the EXAFS and XPS analysis and further confirms that the Ga bonding environment in the $x = 1.5$ sample is identical to that of $GaCl_3$. The heterogeneous elemental distribution, along with the presence of distinct MgF_2 and $GaCl_3$ particles in the $x = 1.5$ sample, indicates that complete anion exchange and phase segregation into the nearly pure halides has occurred. The clay-like $x = 1$ sample, on the other hand, underwent only partial anion exchange and has a uniform elemental distribution. This distinction suggests that the lack of clay-like properties in the $x = 1.5$ sample is due to the completion of the anion exchange reaction and resulting phase segregation. This finding agrees with our observations that mechanochemically mixing the end products (MgF_2 and $GaCl_3$) of the anion exchange reaction failed to yield a clay-like product. Thus, partial anion exchange, which is only observed in the $x = 1$ sample, is crucial to achieve clay-like mechanical properties.

Table 2. A comparison of properties of different structures in Figure S16 (Supporting Information) by trained DeePMD model and DFT (AIMD) calculations.

structure	Property	DFT	DP-MD (LAMMPS)
(a)	Mg-ion conductivity-T=700K	26.4 mS cm^{-1}	27.6 mS cm^{-1}
(a)	Mg-ion conductivity-T=800K	49.7 mS cm^{-1}	50.6 mS cm^{-1}
(b)	Mg-ion conductivity-T=750K	185.2 mS cm^{-1}	189.5 mS cm^{-1}
(c)	Mg-ion conductivity-T=900K	215.5 mS cm^{-1}	219.7 mS cm^{-1}
(a)	Bulk Modulus	16.6 GPa	15.9 GPa
(b)	Bulk Modulus	13.1 GPa	12.6 GPa

To further validate that partial anion exchange is responsible for the soft mechanical behavior in Mg-based clay-like electrolytes, computational analysis was performed using molecular dynamics (MD) simulations with a deep learning-based interatomic potential energy (DeepPE) model. Exploring mechanical behavior and ionic transport in large amorphous structures is intractable with DFT, hence, we use the trained PE model to study these properties. The DeepPE model was trained for the Ga–F–Mg–Cl chemical system using DeepMD.[40] The training was performed using the atomic forces and energies of ab initio molecular dynamics (AIMD) trajectories of 10 stable crystalline phases in the Ga–F–Mg–Cl quaternary chemical space, and 3 slab-like structures of $MgCl_2|GaF_3$ ("|" denotes an interface). The details used for training the interatomic potential energy model are provided in Figure S14 (Supporting Information). The trajectories were obtained by melting and quenching each structure using AIMD simulations (a detailed description of DeepMD training is described in the Experimental Section). Our trained model was validated on a subset of training structures, and the RMSE errors in energy and forces were <1 meV atom^{-1} and <80 meV Å^{-1} after training (Figure S15, Supporting Information). The accuracy of the trained PE model was tested on the atomic forces and energies of several additional structural configurations (Figure S16, Supporting Information) that were not included in the training and validation set. Good agreement was obtained between the atomic forces and energies predicted by the trained PE model and density functional theory (DFT) (Figure S16, Supporting Information). Additionally, the performance of the trained PE model was benchmarked by calculating the bulk modulus and Mg-ion conductivity in 3 slab-like structures of $MgCl_2|GaF_3$ (Figure S16, Supporting Information). **Table 2** presents a comparison of values obtained from the trained PE model and the DFT calculations.

Our experimental analysis indicates that the partial anion exchange that occurs during the ball milling of $MgCl_2$ and GaF_3 may be essential for clay formation, whereas complete anion exchange leads to phase separation without pliability. To emulate the conditions by which $MgCl_2$ and GaF_3 particles react in ball milling in our simulations, we use a previously[34] developed procedure to create a representative amorphous structure containing domains of the constituent particles. The same procedure is adopted here and described in more detail in Experimental Section. First, a supercell containing ≈12 000 atoms with a $MgCl_2$:GaF_3 molar ratio of ≈1:1 was created (Figure S17, Supporting Information), which contains multiple particles of $MgCl_2$

**ADVANCED
SCIENCE NEWS**

www.advancedsciencenews.com

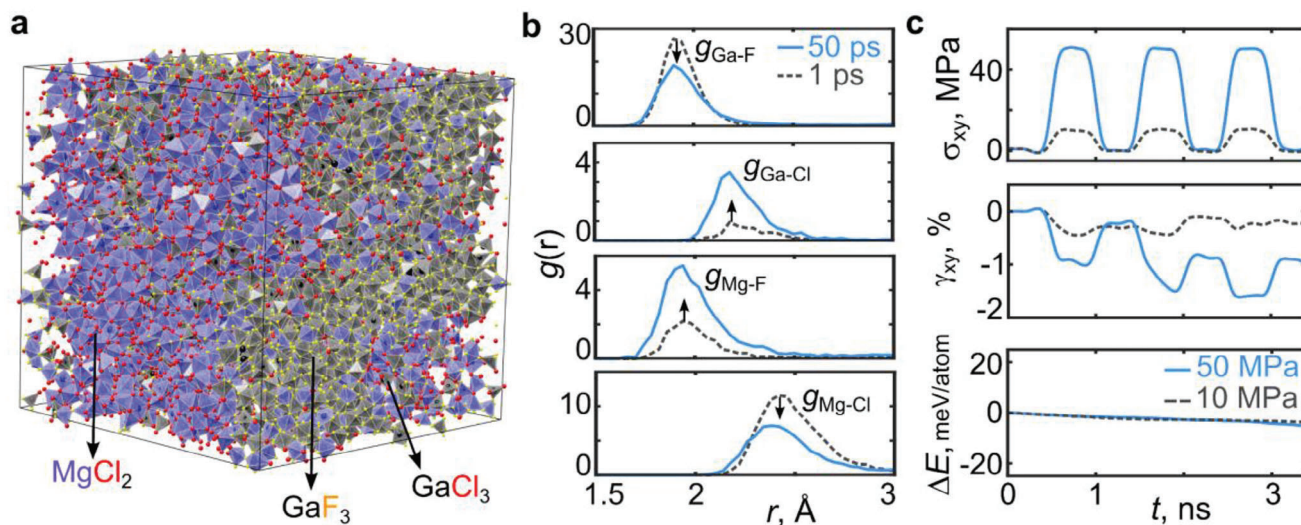**ADVANCED
ENERGY
MATERIALS**

www.advenergymat.de

Figure 4. a) Amorphous Ga–F–Mg–Cl structure, containing domains of $MgCl_2$, GaF_3, and $GaCl_3$-like molecules formed during the high temperature MD simulations; b) Element-wise radial pair distribution function $g(r)$ plotted at $t = 1$ ps and $t = 50$ ps of the MD simulation at $T = 900$ K; c) Applied external shear stress σ_{yz}, accumulated shear strain γ_{yz}, and total potential energy change ΔE of the amorphous structure as a function of time in the MD simulation at $T = 300$ K. The external shear stress ranged from 10 to 50 MPa. The accumulated shear strain after three cycles is non-negligible ($\gamma_{yz} \neq 0$), signifying permanent deformation.

and GaF_3 in contact with each other. The cell was relaxed in LAMMPS[41] using the trained deep-learning based PE model at $T = 0$ K to densify the system. This relaxed cell was subjected to a high-temperature classical MD simulation (hereafter, unless specified, all the MD simulations were performed with LAMMPS using the trained DeepPE model) under the *NVT* ensemble for $t = 50$ ps at $T = 900$ K to allow for some mixing of the atoms. An atomic configuration at $t = 50$ ps was selected and this configuration was relaxed in LAMMPS at $T = 0$ K to a local energy minimum. This procedure is similar to the commonly used melt and quench techniques[42,43] used to create amorphous structures. The relaxed structure was further equilibrated in an MD simulation under the *NPT* ensemble for a duration of 2 ns at $T = 300$ K and zero external stress, until there was no further change in density, lattice constant, angles, or total potential energy. The resulting amorphous structure is shown in **Figure 4a** and exhibits chemical heterogeneity with domains of unreacted $MgCl_2$ and GaF_3, as well as the formation of $GaCl_3$-like units, which are molecular complexes that have a fourfold Ga–Cl tetrahedral coordination similar to that in bulk $GaCl_3$. The observation of $GaCl_3$-like domains is consistent with the experimental XPS and EXAFS results (Figure 3a,b). Figure 4b displays the element-wise radial pair distribution function $g(r)$ before and after the high-temperature ($T = 900$ K) MD simulation of $t = 50$ ps. The Ga–F and Mg–Cl peaks decrease, while the Ga–Cl and Mg–F peaks increase, indicating that anion exchange occurs when the two salts are mixed. This anion exchange is consistent with our experimental spectroscopic observations. The specific volume of the structure was computed at different temperatures, and a glass-like transition was observed at $T_g \approx -53$ °C (Figure S18, Supporting Information), in good agreement with the experimental measurement of $T_g \approx -62$ °C (Figure S2, Supporting Information).

To assess whether the amorphous structure (Figure 4a) is mechanically soft as seen in experiments, a stress-controlled MD simulation was conducted within an *NPT* ensemble at $T = 300$ K. The system was subjected to an external shear stress by setting the xy-component (σ_{xy}) of the stress to either 10 or 50 MPa, while maintaining all other external stress components at zero. This shear stress was applied for a duration of 400 ps, followed by a release phase of 400 ps, and this stress pulse was repeated three times. Figure 4c illustrates the resulting shear strain (γ_{xy}) and the total potential energy (ΔE) of the system. Notably, after undergoing three loading cycles, the cumulative shear strain was non-negligible, indicating permanent deformation and plastic behavior within the structure, even at the relatively low σ_{xy} of 10 MPa. This finding demonstrates that the amorphous structure is mechanically soft, akin to experimental observations. In our prior work on pliable Li electrolytes,[34] the formation of $GaCl_3$-like units during the anion exchange reaction was linked to the soft mechanical response of the material. $GaCl_3$ is a molecular solid (MS), and its inherent softness enables it to act as sites for shear transformation zones and becomes activated at low stress, which leads to soft plastic deformation. In Mg-based clay-like electrolytes, the formation of $GaCl_3$-like molecular solid units is seen in both experiments and simulations. This indicates that the soft plasticity in the Mg-based pliable electrolytes could arise from the formation of MS-like units during the anion exchange reaction, a similar mechanism as that in Li-based pliable electrolytes.

2.4. Computational Simulation of Ionic Transport in Clay-Like Mg-Ion Electrolytes

To study the ion diffusion in the simulated amorphous structure (Figure 4a), we performed a MD simulation in the *NVT* ensemble at $T = 300$ K for $t = 25$ ns. The displacement of all the atoms during the *NVT*-MD simulation was tracked to analyze the ionic
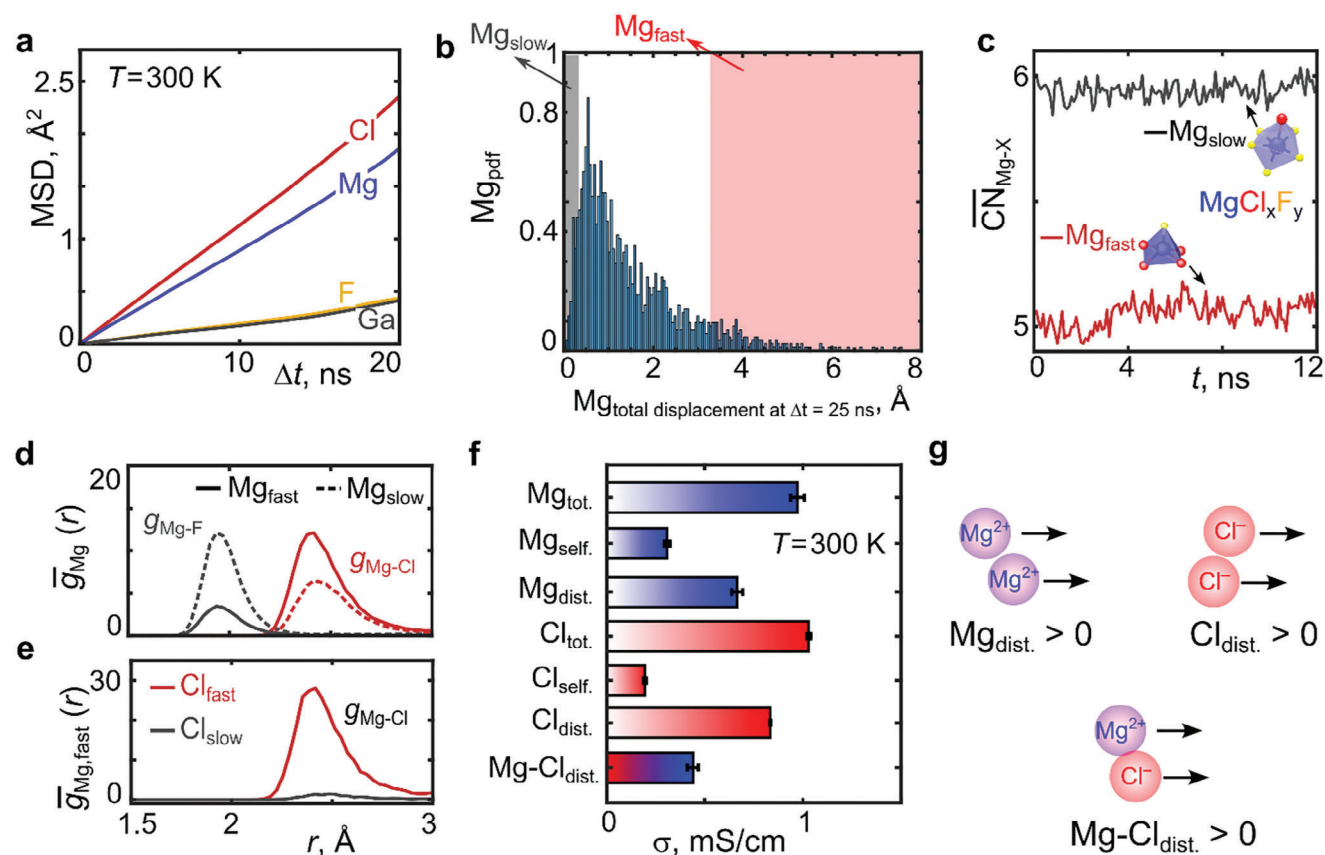
ADVANCED
SCIENCE NEWS
www.advancedsciencenews.com

ADVANCED
ENERGY
MATERIALS
www.advenergymat.de

Figure 5. a) MSD for different ions at time t in amorphous 1MgCl$_2$–GaF$_3$ system; b) Histogram plot showing the distribution of the total displacement at $\Delta t = 25$ ns made by Mg ions, where the histogram bin height h_i is normalized to show a probability density function (pdf) and the bin width w is 0.05 Å. The bin height is normalized as $h_i = c_i/(N \times w)$, where N is the total number of Mg ions and c_i is the number of Mg ions in the ith displacement bin. The product of bin height and width $h_i \times w$ denotes the probability that the Mg ions have that specific displacement. The slow moving Mg$_{slow}$ ions with total displacement <10% of maximum and fast moving Mg$_{fast}$ ions with total displacement >90% of maximum are highlighted by black and red shaded regions, respectively; c) Averaged Mg–X coordination number of fast- and slow-moving Mg ions; d) Element-wise radial pair distribution function $g(r)$ for fast- and slow-moving Mg ions; e) $g(r)$ for fast- and slow-moving Cl ions f) Ionic conductivity of self and distinct contributions from Mg and Cl ions; g) Schematic demonstration of correlated diffusion between Mg–Mg ions, Cl–Cl ions and Mg–Cl ions.

transport properties. **Figure 5a** shows the mean squared displacement (MSD) for the different ions as a function of time t (see Experimental Section for details of the calculation). The MSD increases linearly with time, indicating that a diffusive regime was attained in the simulations. Extracting the self-diffusion coefficient of species, D_s^α, from the slope of the time dependence of the MSD (Equation 1 in Experimental Section), we find $D_s^{Mg} \approx 1.7 \times 10^{-9}$ cm^2 s^{-1}, which corresponds to an ionic conductivity ≈ 0.31 mS cm^{-1} at $T = 300$ K. Interestingly, the Cl ions also display high mobility with $D_s^{Cl} \approx 2.1 \times 10^{-9}$ cm^2 s^{-1}. The ionic conductivity contributed by self-diffusion of individual ions is shown in Table S3 (Supporting Information). To discern any correlation between the fast diffusivity of Mg and Cl ions and their local chemistry, we divided the Mg and Cl ions into fast- and slow-moving species depending on their total displacement after $t = 25$ ns. Figure 5b shows the distribution of the total displacement of Mg ions. Hereafter, fast- and slow-moving Mg and Cl ions refer to the respective atoms with total displacements D >90% of the maximum value and D <10% of the maximum value, respectively. The ratio of the total displacement and mean squared displace-

ment for fast- and slow-moving Mg ions after $t = 25$ ns is ≈ 16 and ≈ 236, respectively. To investigate the difference in the chemical environment for fast- and slow- moving Mg ions, we tracked their Mg–X (X = F, Cl) coordination number (CN$_{Mg-X}$) with time, where CN$_{Mg-X}$ was averaged over all the fast/slow Mg species at each time step. The averaged CN$_{Mg-X}$ for fast-moving Mg$_{fast}$ and slow-moving Mg$_{slow}$ is plotted in Figure 5c. The time-averaged first anion shell CN of fast-moving Mg$_{fast}$ ions is ≈ 5, whereas it is ≈ 6 for slow-moving Mg$_{slow}$ ions. In comparison, the anion coordination number for Mg in bulk MgCl$_2$ and MgF$_2$ is 6. This result indicates that the fast-moving Mg-ions have an undercoordinated chemical environment, whereas the CN of the slow-moving Mg-ions is similar to that in bulk MgF$_2$ and MgCl$_2$. The time averaged pair distribution function $g(r)$ for fast- and slow-moving Mg ions is plotted in Figure 5d. For fast-moving Mg ions, the Mg–Cl peak is higher than the Mg–F peak, while the opposite in the case for the slow-moving Mg ions. To understand if the fast-moving Mg and fast-moving Cl ions are neighbors, we plotted the time averaged hetero-element pair-wise $g(r)$ for Mg$_{fast}$ – Cl$_{fast}$ and Mg$_{fast}$ – Cl$_{slow}$ in Figure 5e. The $g(r)$ peak for Mg$_{fast}$ – Cl$_{fast}$

**ADVANCED
SCIENCE NEWS**

www.advancedsciencenews.com

**ADVANCED
ENERGY
MATERIALS**

www.advenergymat.de

is much higher than that for $Mg_{fast} - Cl_{slow}$, which indicates that the fast-moving Mg ions are coordinated more with fast-moving Cl ions than with slow-moving Cl ions. To verify that the partial anion exchange is critical to promote fast Mg-ion transport, we simulated the polycrystalline system consisting of pure $MgCl_2$ units (a detailed description is described in the Experimental Section; Figure S20, Supporting Information). The polycrystalline $MgCl_2$ structure showed a lower ionic conductivity with an upper bound of 0.05 mS cm^{-1} (Figure S20c, Supporting Information), but detailed analysis (Figure S21, Supporting Information) shows that this conductivity almost exclusively occurs at the boundaries. Hence, the bulk conductivity of $MgCl_2$ is expected to be very low. In contrast, the amorphous $1MgCl_2$–GaF_3 structure exhibits a higher conductivity of 0.31 mS cm^{-1}, and the mobile Mg-ions are not limited to the particle boundaries (Figure S22, Supporting Information).

The behavior of mobile cations and anions in the $1MgCl_2$–GaF_3 amorphous structure resembles features seen in liquid electrolytes, such as molten salts, ionic liquids, and electrolyte solutions,[44–48] where the ions dissociate, and both cations and anions become mobile. Correlation in the motion of Mg and Cl ions is commonly observed in liquid electrolytes.[44–48] To evaluate possible correlation between the Mg and Cl-ions in our clay material, we use the Einstein relation Equation 2, where σ_{tot} includes contributions from all ions, including correlation between their motion (see Experimental Section for the details of the calculation). To quantify the contribution of correlated motion to ionic conductivity, the total conductivity σ_{tot} in Equation 2 can be partitioned into two components: the diagonal components (referred to as the "self" part σ_s), where $i = j$, which represents the diffusion of individual ions, and the off-diagonal components (referred to as the "distinct" part σ_d), where $i \neq j$, arising from correlations between the motions of different ions. The off-diagonal terms include both cross-correlations between ions of the same type and cross-correlations between ions of different types. Figure 5f shows the self and distinct contributions to the ionic conductivity of Mg and Cl. The signs of σ^d_{Mg}, σ^d_{Cl}, and $\sigma^d_{Mg,Cl}$ are positive and their magnitude are greater than those of σ^s_{Mg} and σ^s_{Cl}. The large value of σ^d_{Mg}, σ^d_{Cl}, and $\sigma^d_{Mg,Cl}$ implies that strong correlation exists in the migration of all ions. The positive sign of σ^d_{Mg}, σ^d_{Cl}, and $\sigma^d_{Mg,Cl}$ implies that different ions move in a correlated manner, i.e., different Mg ions move in correlated manner, as well as different Cl-Cl ions, and Mg-Cl ions (Figure 5g). The positive sign of σ^d_{Mg}, and σ^d_{Cl} increases the total conductivity, as different Mg ions move together. The positive sign of $\sigma^d_{Mg,Cl}$, however, decreases the total conductivity, as it indicates that the Mg and Cl ions move with positive correlation, thereby reducing the effective charge being transported. Such correlated motion of cations and anions has also been seen in liquid electrolytes[44–48] and asserts that the ionic transport in amorphous $1MgCl_2$–GaF_3 has features that are analogous to those in liquid electrolytes.

3. Discussion

Achieving both high ionic conductivity and mechanical deformability is important for enabling practical application of solid electrolytes into all-solid-state batteries. In this work, we demonstrate that these two desirable properties can be simultaneously satisfied in a magnesium gallium halide solid in which partial anion exchange has occurred. Specifically, we synthesized a group of clay-like materials from $xMgCl_2$–GaF_3 ($0.75 \leq x \leq 1.25$) precursors by high-energy ball milling. The optimized composition exhibits an RT ionic conductivity of 0.47 mS cm^{-1} and is mechanically soft. This ionic conductivity is among the highest measured for inorganic solid-state Mg-ion conductors at room temperature.[13,14,49,50] The good compressibility and high ion mobility of this material enable the reversible cycling of a solid-state symmetric cell using $Mg_xMo_6S_8$ electrodes without external stack pressure. Our combined experimental characterization and computational modeling strongly suggests that partial anion exchange is the key to both clay formation and the resulting fast ion transport. However, $1MgCl_2$-GaF_3 material was found to have poor interfacial stability with Mg metal. We computationally estimate the electrochemical stability window of $1MgCl_2$-GaF_3 by using a grand potential phase diagram open to Mg. The calculation indicated that $1MgCl_2$-GaF_3 is stable from 1.9 to 3.9 V versus Mg/Mg^{2+}, which implies that this material is more suitable as a catholyte.

The high-energy ball milling promotes the forward reaction $1.5MgCl_2 + GaF_3 \rightarrow 1.5MgF_2 + GaCl_3$, which indeed has a negative ΔH as identified from the Materials Project (Figure S23, Supporting Information). We find that the mixing ratio x of these two precursors greatly impacts the level of anion exchange, which in turn correlates with the mechanical properties of the product. When x is significantly under the stoichiometric value (e.g., $x = 0.5$), the sample remains in the powder state after ball milling because of a relatively low level of anion exchange, as evidenced by the very weak signals of MgF_2 in the synchrotron XRD pattern and the F-dominant environment of Ga atoms as found from XPS and EXAFS analysis. As the mixing ratio x increases, a higher MgF_2 peak intensity is observed in the XRD, and the anion environment of Ga becomes richer in Cl as evidenced by the XPS and EXAFS data for the $x = 1$ and $x = 1.5$ samples. At $x = 1.5$, however, the sample undergoes complete anion exchange and segregates into MgF_2-rich and $GaCl_3$ phases, correlating with a lack of mechanical softness. When x is in the range $0.75 \leq x \leq 1.25$, partial anion exchange occurs during ball mill and the samples exhibit clay-like properties. The formation of $GaCl_3$-like domains within the amorphous matrix is observed both in X-ray spectroscopy and MD simulations. As revealed in previous computational work,[34] the $GaCl_3$-like units can be activated at low stress to form shear transformation zones, leading to soft-plastic deformation.

The importance of the mixing ratio of the precursors for soft-clay formation has also been observed in the analogous lithium system. Mixing a $xLiCl$–GaF_3 sample[29] with $x = 1$ results in a powder-like state, while samples with $2 \leq x \leq 4$ samples form a clay-like state. For the $2LiCl$–GaF_3 sample, partial anion exchange was confirmed with ^{71}Ga NMR, consistent with our observations for $1MgCl_2$–GaF_3 sample. The consistent observation of partial anion exchange in both lithium and magnesium pliable electrolytes indicates that this principle can potentially be exploited to discover novel soft electrolytes for other working ions including sodium and other multivalent ions.

The clay-like $xMgCl_2$–GaF_3 samples exhibit RT ionic conductivity that is approximately three orders of magnitude higher than that of the powdery samples. Our molecular dynamics simulations indicate that the mobility of fast-moving Mg-ion can be

attributed to the undercoordinated environment created by partial anion exchange. A high mobility of undercoordinated ions has been reported in other solid-state conductors including Li-ion in amorphous-LiPON,[51] in solid organic electrolyte,[52] and for the Na-ion in Na_3PS_4.[53] The higher energy related to the undercoordination leads to lower effective hopping barriers, consistent with principles previously elaborated for crystalline conductors.[54,55]

In our simulations of $1MgCl_2$–GaF_3, both cations, and anions show high mobility, and their motions exhibit a strong correlation (Figure 5e). This fast diffusivity of multiple ions in addition to Mg-ion is analogous to what is commonly observed in the liquid and polymer-based electrolytes for magnesium ion batteries.[7,19,56–59] The partial anion exchange between $MgCl_2$ and GaF_3 creates the pliable amorphous matrix, which may serve as a "solvent" to dissociate a Mg-ion to an undercoordinated and chlorine-rich bonding environment. This is similar to the magnesium aluminum chloride complex (MACC) electrolyte. When mixing $MgCl_2$ and $AlCl_3$ in the ether solvent, multiple monomer and dimer Mg–Cl complexes are formed, which contribute to the reversible Mg deposition.[58,60,61] In summary, the Mg-ions in our amorphous system have a heterogeneous coordination environment and display correlated motion with Cl anions.

4. Conclusion

In summary, a ball milled $xMgCl_2$–GaF_3 mixture develops clay-like features and high ionic conductivity when x is in the range $0.75 \leq x \leq 1.25$. The RT ionic conductivity of 0.47 mS cm^{-1} achieved in $1MgCl_2$–GaF_3 is comparable to solid Li-ion electrolytes and would enable this system to serve as a solid electrolyte or catholyte. Through experimental spectroscopy techniques and computational modeling, we demonstrated that partial anion exchange is responsible for the soft mechanical properties. The fast ionic conduction is attributed to the undercoordinated magnesium ions in a chlorine-rich chemical environment.

5. Experimental Section

Synthesis: Mechanochemical ball milling was used to prepare $xMgCl_2$–$1GaF_3$ ($0.5 \leq x \leq 1.5$) samples. $MgCl_2$ (Thermo Invitrogen, 99.9%) and GaF_3 (Thermo Invitrogen, 99.85%) were used as precursors. Stoichiometric amounts of the precursors were dispersed into Ar-filled zirconium oxide ball-mill jars and then planetary ball-milled (Retch PM 200) at 450 rpm for 24 h. In each jar, the total amount of precursors was ≈1 g. Five 10-mm (diameter) and ten 5-mm-(diameter) zirconia balls were used as the grinding media. No Zr contamination was observed from EDS analysis (Figures S12 and S13, Supporting Information) in all the as-synthesized samples. $1.5MgF_2$-$1GaCl_3$ was mechanochemically prepared with MgF_2 (Alfa Aesar, 99.9%), and $GaCl_3$ (Strem Chemicals, ≥99.99%) precursors under the same ball-milling condition.

Morphological and Structural Characterization: The glass transition temperature was determined using a TA Instruments Q200/RCS90 DSC with a heating/cooling rate of 2 °C min^{-1}. The heating–cooling cycle was repeated three times. Approximately 15 mg of sample was loaded and sealed into the DSC pan in an Ar-filled glovebox. SEM images were collected using a Zeiss Gemini Ultra-55 analytical field-emission SEM operated at an applied voltage of 3 kV. EDS was measured with a Bruker X-ray energy dispersive spectrometer coupled to the Ultra-55 SEM at an acceleration voltage of 5 kV. Lab XRD patterns were collected using a Rigaku Mini-Flex diffractometer with Cu Kα radiation. Synchrotron XRD measurements

were performed at beamline 7 BM of NSLS-II, Brookhaven National Laboratory, or Stanford Synchrotron Radiation Lightsource (SSRL) beamline 2-1 with wavelengths of 0.6199 and 0.7273 Å respectively. All the samples were covered with Kapton tape to avoid air exposure.

Electrochemistry: The Mg-ion conductivity was evaluated using EIS analysis. The clay-like electrolytes were rolled into films and cut into a round piece with a 7/32-inch punch, which was then sandwiched between two platinum foils for EIS measurement. The Pt|$xMgCl_2$–$1GaF_3$|Pt assembly was sealed in a Swagelok-type cell in an Ar-filled glovebox. Powder-state samples were uniaxially compressed under a pressure of ≈300 MPa with two gold-sputtered stainless-steel rods as blocking electrodes. The sputtered 15-nm gold layer was added to prevent side reaction between the sample and stainless-steel rod. EIS measurements were performed using an EC-Lab Electrochemistry SP300 system. The measurements were conducted at the initial open-circuit voltage in the frequency range of 7 MHz–10 mHz with application of a 10 mV signal amplitude. EIS data fitting was performed using the ZView software package. The electronic conductivity was measured by DC polarization, during which a constant voltage of 0.5 V versus the open circuit was applied to all the cells. The symmetric solid-state cell was constructed by attaching a pristine Mo_6S_8 film as the cathode and a discharged $Mg_xMo_6S_8$ film as the anode to the $1MgCl_2$–$1GaF_3$ electrolyte. Chevrel phase Mo_6S_8 was synthesized using the method from ref. [36]. Stoichiometric amounts of MoS_2, Mo, and CuS were milled for 2 h in a SPEX-8000 M Mixer, which was then annealed at 1010 °C for 8 h under an argon atmosphere to form $CuMo_6S_8$. The copper-ions were leached using 6 M hydrochloric acid under oxygen flow for 9 h. The acid solution was centrifuged, washed with deionized water three times, and dried in the oven to obtain Mo_6S_8 powder. To prepare the cathode film, the Mo_6S_8 powder, carbon black (Timcal, SUPER C65), and PTFE (Dupont, Teflon 8C) were mixed in a weight ratio of 7:2:1 using a mortar and pestle and rolled into a thin film inside an Ar-filled glove box. To obtain the $Mg_xMo_6S_8$ film, the cathode film was discharged to −1.5 V versus the activated carbon anode in a coin cell with liquid electrolyte, 0.5 M Mg(TFSI)$_2$ in acetonitrile. Residual liquid electrolyte was removed by rinsing in the acetonitrile and drying overnight. The capacity of the $Mg_xMo_6S_8$ anodes was in ≈1.25-fold excess of the Mo_6S_8 cathodes.

Extended X-Ray Absorption Fine Structure Spectroscopy and X-Ray Photoelectron Spectroscopy: Ga K-edge EXAFS was performed at beamline 7 BM of NSLS-II, Brookhaven National Laboratory. The measurements were performed in transmission mode using a Si (111) monochromator. A Rhenium foil (10 535 eV) was simultaneously measured to calibrate the energy of the individual datasets. To prevent air exposure, the samples were sealed between polyimide tape. The EXAFS spectra of the Ga edge were calibrated and normalized using the Athena software.[62] The background contribution was limited below a radial distance (Rbkg) = 1.0 using the built-in AUTOBK algorithm. The extracted EXAFS signal was weighted by k^3 to accentuate the high-energy oscillations and then Fourier-transformed using a Hanning window function to plot the spectra in R-space. Because the Fourier transform was not phase corrected, the R values obtained from the Fourier transform are shorter than the actual distances.[63] XPS measurement was performed on a Thermofisher K-Alpha Plus XPS using AlKα radiation. All the measured samples were placed on the silver tape in the argon glovebox and transferred to the XPS equipment using an evacuated device to avoid air exposure. The binding energies were calibrated from the C 1s XPS peak (284.8 eV) as the internal standard reference.

Training Deep Learning-Based Interatomic Potential: The deep learning-based interatomic potential energy (PE) model for the Ga–F–Mg–Cl chemical system was trained using the Smooth Edition[64] version 2.1.5 of the DeepMD-kit[65] package. The *embedding* net and *fitting* net sizes were (24, 48, 96) and (240, 240, 240), respectively. The cut-off radius r_{cut} was 8.5 Å and the smoothing parameter r_{cut_smth} was set to 5.5 Å. The fitting network was trained by minimizing the loss function $L = p_eL_e + p_fL_f$, where L_e and L_f were the loss in energy and force, respectively, and p_e and p_f were the corresponding prefactors varying from 0.02 to 1 and 1000 to 1, respectively. In the minimization of the loss function, the exponential learning rate decayed every *decay_steps* of 5000 from an initial value of 0.001. A total number of 7×10^5 iterations of training batches (minimization steps) were used to produce the final DeepMD PE model, until the root mean square

error (RMSE) in energy and forces became constant, with the RMSE values for energy and forces being <1 meV atom^{-1}, and <80 meV Å^{-1}, respectively (see Figure S15, Supporting Information).

The DeepMD PE model was trained using atomic configurations obtained from the AIMD simulation frames of various stable structures in the Ga–F–Mg–Cl quaternary chemical space and slab-like structures of MgCl$_2$|GaF$_3$ (where a multilayer slab of [001] MgCl$_2$ and [001] GaF$_3$ is interfaced "|") as illustrated in Figure S14 and Table S2 (Supporting Information). To generate atomic configurations for the training data, a melt and quench strategy was used. Each structure was heated in AIMD simulations at a constant rate from $T = 0$ K to the respective highest temperature as shown in Table S2 (Supporting Information) for 10 ps in the NVT ensemble and a time step of 2 fs. Subsequently, the temperature was kept constant for 30 ps, after which the structure was cooled from the highest temperature to $T = 0$ K in 10 ps under a constant cooling rate. Additionally, to sample a larger configuration space and incorporate the effect of volume change, AIMD simulations were performed at high temperatures as shown in Table S2 (Supporting Information) in the NPT ensemble with a time step of 2 fs. In total, over 700k AIMD frames were generated, out of which 200k atomic configurations were randomly selected to train the DeepMD PE model. Among the 200k configurations, 80% of them were used for training and 20% for validation.

Density Functional Theory Calculations: First-principles density functional theory (DFT) calculations were performed for structural relaxation and obtain the bulk modulus of the compounds investigated in this work. All the calculations were performed using the Vienna Ab initio Simulation Package[66] (VASP) version 6.2. Ion-electron interactions were represented by projector augmented wave potentials.[67] The generalized gradient approximation (GGA) parameterized by Perdew-Burke-Ernzerhof[68] (PBE) was used to account for the electronic exchange and correlation. The DFT-D2 method of Grimme was used to include the Van der Waals interaction. The wave functions were expanded in a plane wave basis with an energy cut-off of 500 eV and a reciprocal-space discretization of at least 30 k-points per Å^{-1} was used to sample the Brillouin Zone. The convergence criteria were set as 10^{-6} eV for electronic loops and 0.01 eV Å^{-1} for ionic loops. Ab initio molecular dynamics (AIMD) simulations were performed to generate atomic configurations for the training datasets as well as to obtain Mg-ion conductivities for benchmarking the trained DeepMD PE model. A gamma-point-only sampling of k-space, a plane-wave energy cutoff of 500 eV, and a time step of 2 fs were used. NVT ensemble calculations were performed with the Nosé-Hoover thermostat, whereas the NPT ensemble calculations were conducted using the Langevin thermostat in non-spin mode. The electrochemical stability window of the amorphous 1MgCl$_2$-GaF$_3$ was determined computationally by constructing a T = 0 K grand potential phase diagram for various Mg chemical potentials and finding the range of Mg chemical potential where the amorphous material was stable. This was achieved with a procedure outlined in prior work[69] and the use of Pymatgen.[70]

Classical Molecular Dynamics: LAMMPS[41] package was used to perform classical MD simulations using the trained DeepMD interatomic potential energy model of the Ga–F–Mg–Cl chemical space. All MD simulations were performed in either the NVT or NPT ensembles (as specified). The Nosé-Hoover thermostat and a time step of 1 fs were used. The T_{damp} and P_{damp} parameters were set to 0.2 ps and 1 ps, respectively. In the constant-stress MD simulations (Figure 4c), the fluctuations in the applied external shear stress σ_{yz}, accumulated shear strain γ_{yz}, and total potential energy E were removed by replacing the value of each quantity (σ_{yz}, $\gamma\gamma_{yz}$, and E) at time t by its average value over a time interval of $[t - \Delta t, t + \Delta t]$, where $\Delta t = 5$ ps. Figure 4c shows the values after this averaging.

Generating the Amorphous Structure: To create the amorphous structure, a similar procedure as that developed earlier[34] for pliable Li-based electrolytes was used. We first created a slab-like geometry of MgCl$_2$|GaF$_3$, where a multilayer slab of [001] MgCl$_2$ and [001] GaF$_3$ was interfaced in a MgCl$_2$:GaF$_3$ molar ratio of ≈1. This slab-like structure was subjected to an AIMD simulation under the NVT ensemble for $t = 5$ ps at $T = 900$ K to equilibrate the interface, and then relaxed at $T = 0$ K to a local energy minimum. The resulting structure, as shown in Figure S17a (Supporting Information), was then periodically repeated along the two directions per-

pendicular to the interface, and a ≈3 nm cubic "particle" was cut out from it. Eight of these identical ≈3 nm aperiodic particles, adding up to ≈12k atoms, were arranged in a larger cell of size ≈6.4 nm (Figure S17b, Supporting Information). To achieve many distinct interfacial environments, each of the ≈3 nm particles was rotated 90° with respect to their neighbors, such that the axis normal to the interface between MgCl$_2$ and GaF$_3$ in each particle did not align in the same direction as that of the neighboring particles. To create a representative structure of polycrystalline MgCl$_2$, a similar procedure is adopted. First, a cubic supercell with a cell length of 6.4 nm and 10200 atoms (Figure S20, Supporting Information) was created. This supercell contains multiple particles of MgCl$_2$ in contact with each other. The cell was relaxed in LAMMPS using the trained deep-learning based PE model at $T = 0$ K to densify the system. The relaxed structure was further equilibrated in an MD simulation under the NPT ensemble for a duration of 2 ns at $T = 300$ K and zero external stress until there was no further change in density, lattice constant, angles, or total potential energy.

Mean Squared Displacement: The self-diffusion coefficient of species α $D_{s,\alpha}$ is proportional to the slope of the time dependence of the mean squared displacement (MSD) and is given by Equation (1):

$$D_{s,\alpha} = \frac{1}{6N_\alpha} \lim_{t\to\infty} \frac{d}{dt} \left\langle \sum_i \left[r_i^\alpha(t) - r_i^\alpha(0) \right]^2 \right\rangle \tag{1}$$

where, $r_i^\alpha(t)$ is the position of the i-th ion of species α at time t relative to the system center-of-mass, N_α is the total number of ions of species α, and the brackets $\langle\rangle$ denote the ensemble average. The term in brackets divided by N_α is the MSD of species α at time t. Figure 5a shows the ensemble averaged mean squared displacement of all the ions as a function of time t. Ensemble averaging was done by following a previously reported procedure.[71]

Ionic Conductivity: To evaluate the ionic conductivity σ of the system, we use the Einstein relation where σ includes the effects due to correlations between the motion of ions Equation (2):

$$\sigma_{tot} = \frac{e^2}{6Vk_BT} \lim_{t\to\infty} \frac{d}{dt} \left\langle \sum_{i,j}^N z_i z_j \left[r_i(t) - r_i(0) \right] \cdot \left[r_j(t) - r_j(0) \right] \right\rangle \tag{2}$$

In Equation 2, V is the volume of the simulation box; k_B is Boltzmann's constant; T is the temperature, e is the elementary charge; z_i and z_j are the charges of ions i and j, respectively; N is the total number of ions (including all types of species) in the system, and the term in the angular bracket "<>" without the charges was called the collective squared displacement (CSD). The position of ions in the MD trajectories and Equation 2 was used to calculate the conductivity of the system at $T = 300$ K. Figure S19 (Supporting Information) shows the collective squared displacement (CSD) of the different ions species as a function of time. The CSD is linear with time, indicating that a diffusive regime was reached in the simulations.

σ_{tot} in Equation 2 can be rewritten as a sum of "self" σ_s and "distinct" σ_d contributions of the different ions (Equation 3). The "self" part refers to the diagonal components, where $i = j$ and represents the diffusion of individual ions (Equation 4), while the "distinct" part refers to the off-diagonal components, $i \neq j$ representing the correlation between the motions of different ions (Equation 5). The expressions below are written for generic species α and β Equations (3)–(7).

$$\sigma_{tot} = \sigma_{Mg}^s + \sigma_{Mg}^d + \sigma_{Cl}^s + \sigma_{Cl}^d - 2\sigma_{Mg,Cl}^d + \sigma_{Ga}^s + \sigma_{Ga}^d + \sigma_F^s + \sigma_F^d - 2\sigma_{Ga,F}^d$$
$$+ 2\sigma_{Mg,Ga}^d - 2\sigma_{Mg,F}^d - 2\sigma_{Ga,Cl}^d + 2\sigma_{F,Cl}^d \tag{3}$$

$$\sigma_\alpha^s = \frac{|z_\alpha|^2 e^2}{6Vk_BT} \lim_{t\to\infty} \frac{d}{dt} \left\langle \sum_i^{N_\alpha} \left[r_i^\alpha(t) - r_i^\alpha(0) \right] \cdot \left[r_i^\alpha(t) - r_i^\alpha(0) \right] \right\rangle \tag{4}$$

$$\sigma_\alpha^d = \frac{|z_\alpha|^2 e^2}{6Vk_BT} \lim_{t\to\infty} \frac{d}{dt} \left\langle \sum_{i\in\alpha}^{N_\alpha} \left[r_i^\alpha(t) - r_i^\alpha(0) \right] \cdot \sum_{j\in\alpha\neq i}^{N_\alpha} \left[r_j^\alpha(t) - r_j^\alpha(0) \right] \right\rangle \tag{5}$$

**ADVANCED
SCIENCE NEWS**

www.advancedsciencenews.com

**ADVANCED
ENERGY
MATERIALS**

www.advenergymat.de

$$\sigma_\alpha^{tot} = \sigma_\alpha^s + \sigma_\alpha^d \qquad (6)$$

$$\sigma_{\alpha,\beta}^d = \frac{|z_\alpha||z_\beta|e^2}{6Vk_BT} \lim_{t\to\infty} \frac{d}{dt} \left\langle \sum_{i\in\alpha}^{N_\alpha} \left[r_i^\alpha(t) - r_i^\alpha(0) \right] \cdot \sum_{j\in\beta}^{N_\beta} \left[r_j^\beta(t) - r_j^\beta(0) \right] \right\rangle \qquad (7)$$

Supporting Information

Supporting Information is available from the Wiley Online Library or from the author.

Conflict of Interest

The authors declare no conflict of interest.

Data Availability Statement

The data that support the findings of this study are available from the corresponding author upon reasonable request.

[1] J. Xu, X. Cai, S. Cai, Y. Shao, C. Hu, S. Lu, S. Ding, *Energy Environ. Mater.* **2022**, *6*, e12450.

[2] Y. Tian, G. Zeng, A. Rutt, T. Shi, H. Kim, J. Wang, J. Koettgen, Y. Sun, B. Ouyang, T. Chen, Z. Lun, Z. Rong, K. Persson, G. Ceder, *Chem. Rev.* **2021**, *121*, 1623.

[3] Y. Chen, C. J. Bartel, M. Avdeev, Y.-Q. Zhang, J. Liu, P. Zhong, G. Zeng, Z. Cai, H. Kim, H. Ji, G. Ceder, *Chem. Mater.* **2022**, *34*, 128.

[4] J. Muldoon, C. B. Bucur, T. Gregory, *Chem. Rev.* **2014**, *114*, 11683.

[5] Z. Liang, C. Ban, *Angew. Chem., Int. Ed. Engl.* **2021**, *60*, 11036.

[6] N. N. Rajput, T. J. Seguin, B. M. Wood, X. Qu, K. A. Persson, *Top Curr. Chem. (Cham)* **2018**, *376*, 19.

[7] N. N. Rajput, X. Qu, N. Sa, A. K. Burrell, K. A. Persson, *J. Am. Chem. Soc.* **2015**, *137*, 3411.

[8] Y. Zhan, W. Zhang, B. Lei, H. Liu, W. Li, *Front. Chem.* **2020**, *8*, 125.

[9] B. Zhou, H. Shi, R. Cao, X. Zhang, Z. Jiang, *Phys. Chem. Chem. Phys.* **2014**, *16*, 18578.

[10] Y. Gao, T. P. Mishra, S.-H. Bo, G. Sai Gautam, P. Canepa, *Annu. Rev. Mater. Res.* **2022**, *52*, 129.

[11] Z. A. Halim, S. B. R. S. Adnan, F. M. Salleh, N. S. Mohamed, *J. Magnes. Alloy* **2017**, *5*, 439.

[12] S. Ikeda, M. Takahashi, J. Ishikawa, K. Ito, *Solid State Ionics* **1987**, *23*, 125.

[13] K. Kisu, S. Kim, M. Inukai, H. Oguchi, S. Takagi, S. Orimo, *ACS Appl. Energy Mater.* **2020**, *3*, 3174.

[14] E. Roedern, R.-S. Kühnel, A. Remhof, C. Battaglia, *Sci. Rep.* **2017**, *7*, 46189.

[15] Y. Yan, W. Dononelli, M. Jørgensen, J. B. Grinderslev, Y.-S. Lee, Y. Whan Cho, R. Černý, B. Hammer, T. R. Jensen, *Phys. Chem. Chem. Phys.* **2020**, *22*, 9204.

[16] L.-P. Wang, Z. Zhao-Karger, F. Klein, J. Chable, T. Braun, A. R. Schür, C.-R. Wang, Y.-G. Guo, M. Fichtner, *ChemSusChem* **2019**, *12*, 2286.

[17] P. Canepa, S.-H. Bo, G. Sai Gautam, B. Key, W. D. Richards, T. Shi, Y. Tian, Y. Wang, J. Li, G. Ceder, *Nat. Commun.* **2017**, *8*, 1759.

[18] X. Ge, F. Song, A. Du, Y. Zhang, B. Xie, L. Huang, J. Zhao, S. Dong, X. Zhou, G. Cui, *Adv. Energy Mater.* **2022**, *12*, 2201464.

[19] R. Manjuladevi, S. Selvasekarapandian, M. Thamilselvan, R. Mangalam, S. Monisha, P. C. Selvin, *Ionics* **2018**, *24*, 3493.

[20] Y. Yoshida, T. Yamada, Y. Jing, T. Toyao, K. Shimizu, M. Sadakiyo, *J. Am. Chem. Soc.* **2022**, *144*, 8669.

[21] P. W. Jaschin, Y. Gao, Y. Li, S.-H. Bo, *J. Mater. Chem. A* **2020**, *8*, 2875.

[22] Y. Yan, J. B. Grinderslev, M. Jørgensen, L. N. Skov, J. Skibsted, T. R. Jensen, *ACS Appl. Energy Mater.* **2020**, *3*, 9264.

[23] C. Glaser, Z. Wei, S. Indris, P. Klement, S. Chatterjee, H. Ehrenberg, Z. Zhao-Karger, M. Rohnke, J. Janek, *Adv. Energy Mater.* **2023**, *13*, 2301980.

[24] X. Miao, H. Wang, R. Sun, C. Wang, Z. Zhang, Z. Li, L. Yin, *Energy Environ. Sci.* **2020**, *13*, 3780.

[25] S. Su, J. Ma, L. Zhao, K. Lin, Q. Li, S. Lv, F. Kang, Y.-B. He, *Carbon Energy* **2021**, *3*, 866.

[26] B. Tao, D. Zhong, H. Li, G. Wang, H. Chang, *Chem. Sci.* **2023**, *14*, 8693.

[27] Y. Nikodimos, W.-N. Su, B. J. Hwang, *Adv. Energy Mater.* **2023**, *13*, 2202854.

[28] X. Nie, J. Hu, C. Li, *Interdiscip. Mater.* **2023**, *2*, 365.

[29] S.-K. Jung, H. Gwon, G. Yoon, L. J. Miara, V. Lacivita, J.-S. Kim, *ACS Energy Lett.* **2021**, *6*, 2006.

[30] F. Li, X. Cheng, G. Lu, Y.-C. Yin, Y.-C. Wu, R. Pan, J.-D. Luo, F. Huang, L.-Z. Feng, L.-L. Lu, T. Ma, L. Zheng, S. Jiao, R. Cao, Z.-P. Liu, H. Zhou, X. Tao, C. Shang, H.-B. Yao, *J. Am. Chem. Soc.* **2023**, *145*, 27774.

[31] S. Zhang, F. Zhao, J. Chen, J. Fu, J. Luo, S. H. Alahakoon, L.-Y. Chang, R. Feng, M. Shakouri, J. Liang, Y. Zhao, X. Li, L. He, Y. Huang, T.-K. Sham, X. Sun, *Nat. Commun.* **2023**, *14*, 3780.

[32] R. Xu, J. Yao, Z. Zhang, L. Li, Z. Wang, D. Song, X. Yan, C. Yu, L. Zhang, *Adv. Sci.* **2022**, *9*, 2204633.

[33] A. Jain, S. P. Ong, G. Hautier, W. Chen, W. D. Richards, S. Dacek, S. Cholia, D. Gunter, D. Skinner, G. Ceder, K. A. Persson, *APL Mater. Mater.* **2013**, *1*, 011002.

[34] S. Gupta, X. Yang, G. Ceder, *Nat. Commun.* **2023**, *14*, 6884.

[35] R. A. Huggins, *Ionics* **2002**, *8*, 300.

[36] P. Saha, M. K. Datta, O. I. Velikokhatnyi, A. Manivannan, D. Alman, P. N. Kumta, *Prog. Mater. Sci.* **2014**, *66*, 1.

[36] P. Saha, P. H. Jampani, M. K. Datta, D. Hong, B. Gattu, P. Patel, K. S. Kadakia, A. Manivannan, P. N. Kumta, *Nano Res.* **2017**, *10*, 4415.

[37] D. Aurbach, Z. Lu, A. Schechter, Y. Gofer, H. Gizbar, R. Turgeman, Y. Cohen, M. Moshkovich, E. Levi, *Nature* **2000**, *407*, 724.

[38] M. D. Levi, E. Lancry, H. Gizbar, Z. Lu, E. Levi, Y. Gofer, D. Aurbach, *J. Electrochem. Soc.* **2004**, *151*, A1044.